An $[Fe^{III}_{30}]$ molecular metal oxide

Alice E. Dearle,[|a] Daniel J. Cutler,[|a] Marco Coletta,[|a] Edward Lee,[|b] Sourav Dey,[c] Sergio Sanz,[a] Hector W. L. Fraser,[a] Gary S. Nichol,[a] Gopalan Rajaraman,*[c] Jürgen Schnack,*[d] Leroy Cronin*[b] and Euan K. Brechin*[a]

[a]*Ms A. Dearle, Dr M. Coletta, Mr D. J. Cutler, Dr H. Fraser, Dr G. S. Nichol, Prof E. K. Brechin, EaStCHEM School of Chemistry, The University of Edinburgh, David Brewster Road, Edinburgh, EH9 3FJ, UK. E-mail: E.Brechin@ed.ac.uk*

[b]*Dr E. Lee, Prof L. Cronin, WestCHEM School of Chemistry, The University of Glasgow, University Avenue, Glasgow, G12 8QQ, UK. E-mail: Lee.Cronin@glasgow.ac.uk.*

[c]*Mr S. Dey, Prof G. Rajaraman, Department of Chemistry, Indian Institute of Technology Bombay, Mumbai, 400076, India. Email: rajaraman@chem.iitb.ac.in*

[d]*Prof J. Schnack, Fakultät für Physik, Universitat Bielefeld, Postfach 100131, D-33501 Bielefeld, Germany. Email: jschnack@uni-bielefeld.de*

[|] Contributed equally.

Abstract

Dissolution of $FeBr_3$ in a mixture of acetonitrile and 3,4-lutidine in the presence of an amine results in the formation of an $[Fe_{30}]$ molecular metal oxide containing alternating layers of tetrahedral and octahedral Fe^{III} ions. Mass spectrometry suggests the cluster is formed quickly and remains stable in solution, while magnetic measurements and DFT calculations reveal competing antiferromagnetic exchange interactions.

Introduction

The diverse chemistry of the earth abundant Fe ion remains at the forefront of a variety of transformative scientific disciplines, including biochemistry,[1] catalysis,[2] porous materials,[3] nanoparticles,[4] batteries,[5] superconductivity,[6] thermoelectrics,[7] spintronics,[8] and magnetism.[9] In the latter area Fe remains ubiquitous in both solid-state[10] and molecule-based chemistry.[11,12]

The recent discoveries of three molecular iron oxide compounds, $[Fe_{13}]$,[13,14] $[Fe_{17}]$,[15] and $[Fe_{34}]$,[16] with structures related to the minerals ferrihydrite and magnetite, suggests that several other very large, high symmetry, molecular clusters exist en route to the formation of 3D oxide or oxyhydroxide mineral phases. In turn, this hints that (large) lacunary or diminished molecular oxyhydroxide [FeO(OH)] clusters not conforming to mineral structure types, including heterometallic species, must also exist. The plausibility of this concept is further supported by the existence of the iron storage protein ferritin which holds ~4,500 Fe^{III} ions in a molecular ferrihydrite cluster in the inner wall of its spherical shell.[17]

The synthetic procedures used to make $[Fe_{13},]$, $[Fe_{17},]$ and $[Fe_{34}]$ are remarkably straightforward. For example, $[Fe_{17}]$ is made by dissolving anhydrous $FeBr_3$ in wet pyridine (py) (or from a combination of pyridine with a second co-solvent).[15] $[Fe_{34}]$ comes from an analogous reaction to $[Fe_{17}]$ but with a different solvent ratio and in the presence of an additional base/templating agent.[16] The wet pyridine acts as a solvent, a source of H_2O (O^{2-}, OH^-), base, ligand, and cation (pyH^+). Charge balancing anions originate from the salt employed. Interestingly, in the formation of the $[Fe_{17}]$ cage the py can be replaced with a number of different analogues, including 4-ethylpyridine, β-picoline, 3,5-lutidine, and isoquinoline, reflecting the relative stability of the compound.[15]

Results and discussion

In order to explore this reaction space more efficiently we initially turned to an automated robotic crystallisation platform which methodically explored the combination of multiple reactants under a range of conditions. Initial results indicated the presence of crystalline species containing up to 36 Fe^{III} ions. Further manual examination revealed that the dissolution of $FeBr_3$ in a 3,4-lutidine (lut)/acetonitrile solution, in the presence of hexamethylenetetramine (HMTA) results in the formation of (lutH)[Fe^{III}_{30}(μ_4-O)$_6$(μ_3-O)$_{26}$(μ-OH)$_{15}$Br$_9$(lut)$_{15}$]Br$_3$ (**1**, Figure 1; Table S1). A similar reaction replacing the 3,4-lutidine with 4-ethylpyridine (Et-py) affords the isostructural species (Et-pyH)[Fe^{III}_{30}(μ_4-O)$_6$(μ_3-O)$_{26}$(μ-OH)$_{15}$Br$_9$(Et-py)$_{15}$]Br$_3$ (**1a**). See the SI for details. For the sake of brevity, we restrict all further discussion to complex **1**.

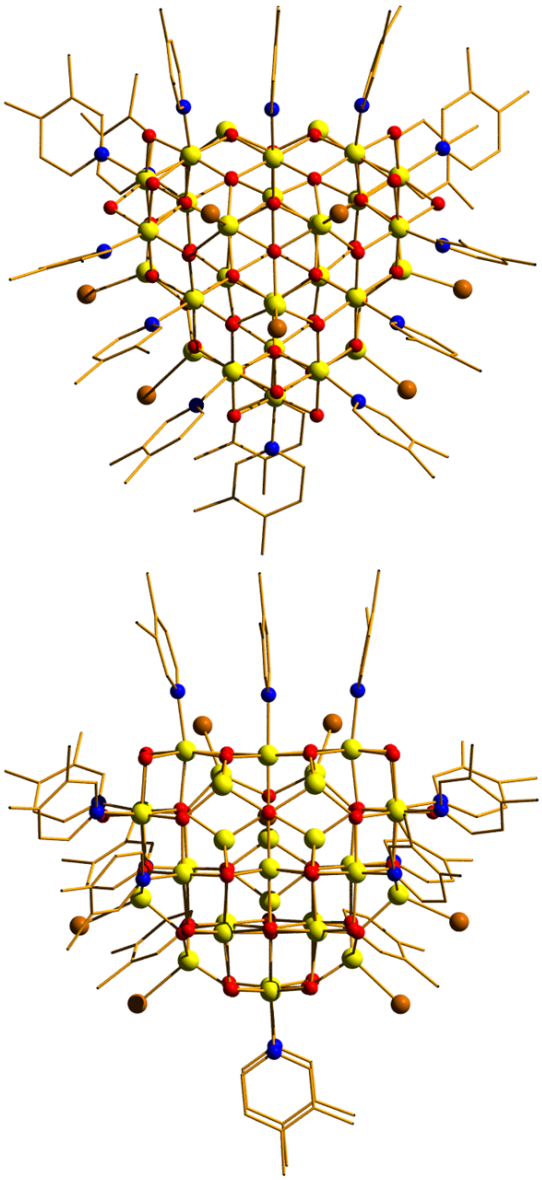

Fig. 1. Orthogonal views of the molecular structure of the cluster cation of **1**. Colour code: Fe = yellow, O = red, N = blue, C = black, Br = brown. H atoms, lutH cations and Br anions omitted for clarity.

Compound **1** crystallises in the monoclinic space group *Pn* with two [Fe_{30}] complexes in the asymmetric unit. The metallic skeleton of the [Fe_{30}] cage (Figure 2, S1) is constructed from alternate layers of tetrahedral and octahedral Fe^{III} ions. In the centre of the cage is a [Fe^{III}_3] triangle of tetrahedral Fe ions.

This is surrounded by a partial [Fe^{III}_{18}] supertetrahedron of octahedral Fe ions – in which three of the corners are truncated into three-membered rings, and one corner is truncated into a six membered ring. The [Fe^{III}_{18}] cage is surrounded by a partial [Fe^{III}_{9}] cuboctahedron of tetrahedral Fe ions. Thus, in total, there are twelve tetrahedral Fe^{III} sites and eighteen octahedral Fe^{III} sites. The Fe ions in the inner [$Fe^{III}_{3}O_9$]$^{18-}$ triangle are linked to each other and to the metal ions in the [Fe^{III}_{18}] unit through six μ_4- and three μ_3-O^{2-} ions. Twenty two μ_3-O^{2-} ions then link the octahedral Fe ions in the [$Fe^{III}_{18}O_{22}$]$^{12+}$ unit to each other and to the tetrahedral Fe ions in the outer [Fe^{III}_{9}] partial cuboctahedron. The remaining μ_3-O^{2-} ions link three tetrahedral Fe ions in the [Fe^{III}_{9}] partial cuboctahedron. The fifteen hydroxide ions are all located in the [Fe^{III}_{18}] cage and are of two types: six are μ-bridging between Fe ions in the [Fe_6] ring and the remaining nine are μ-bridging between Fe ions in the [Fe_3] rings. The monodentate 3,4-tutidine ligands are all bonded to octahedral Fe ions in the [Fe^{III}_{18}] moiety, while the nine tetrahedral iron ions in the outer partial [Fe^{III}_{9}] cuboctahedron are each capped by a terminal Br ion. The Fe-O-Fe angles fall into two distinct categories: those connecting the tetrahedral metal ions to tetrahedral/octahedral metals ions are much larger (115.5(7)-134.9(6)°) than those connecting octahedral metal ions to other octahedral metal ions (90.1(5)-104.9(6)°). The [Fe_{30}] cage has an overall charge of 2+, balanced by the presence of three Br counter anions (H-bonded to the μ-OH ions associated with the truncated [Fe_3] rings (Figures S2-3), OH···Br, ~3.3 Å), and one lutH cation. The closest inter-cluster interactions occur between neighbouring Me (lut) groups (C···C, ~3.2-3.6 Å) and between the terminal Br ions and Me(lut) groups (Br···C, ~3.2-3.6 Å).

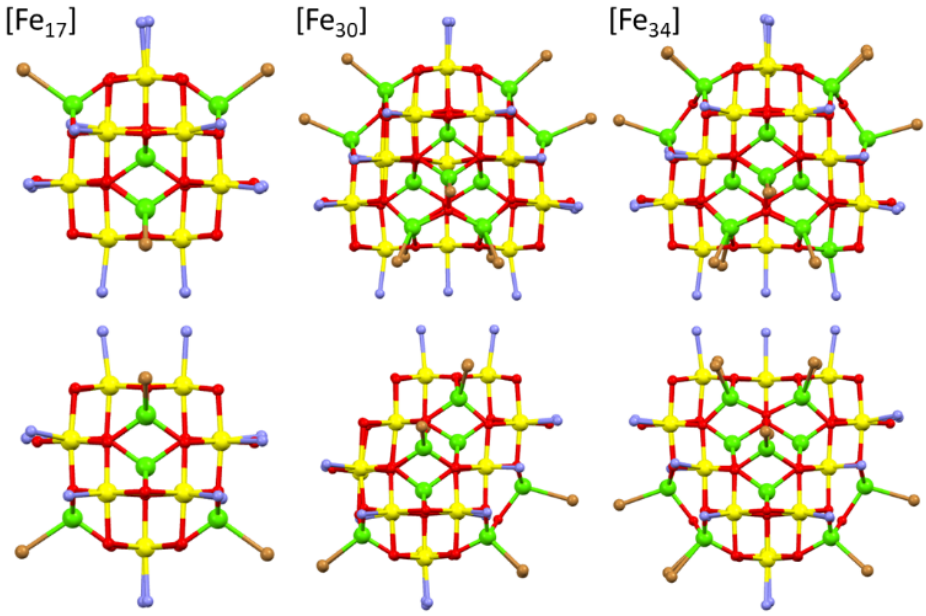

Fig. 2. A comparison of the core structures of [Fe_{17}] (left), [Fe_{30}] (middle) and [Fe_{34}] (right). The bottom panel shows the same figures as the upper panel, but rotated 90°. The tetrahedral Fe ions are in green and the octahedral Fe ions are in yellow, highlighting the structural similarity and growth of the metal-oxygen cores. Figures not to scale. Remaining colour code as Figure 1.

A structural comparison to the previously published molecular Fe oxides [Fe_{17}] and [Fe_{34}] (Figure 2) and to the [Fe_{13}] Keggin ion, shows some striking similarities. In each case the cluster is built up from alternate layers of tetrahedral and octahedral Fe ions. In [Fe_{13}] and [Fe_{17}] there is a single tetrahedral Fe ion in the centre, surrounded by a truncated tetrahedron of octahedral metal ions. [Fe_{17}] has an additional outer shell of four tetrahedral metal ions arranged in a tetrahedron. [Fe_{34}] contains a central

tetrahedron of tetrahedral metal ions, surrounded by a truncated tetrahedron of octahedral metals ions, surrounded by a truncated tetrahedron of tetrahedral metal ions. [Fe_{30}] has a central triangle of tetrahedral metal ions, rather than a tetrahedron, which clearly modifies the subsequent self-assembly process. The resultant changes in structure and symmetry have significant consequences for the magnetic behaviour (*vide infra*). The structural similarities across the [Fe_{13}], [Fe_{17}], [Fe_{30}] and [Fe_{34}] series, and to Fe mineral phases such as ferrihydrite, do therefore hint that the growth of these complexes occurs layer by layer through addition of polynuclear building blocks.

Mass spectrometry (see the SI for full details) of the initial reaction solution indicates that the [Fe_{30}] species is formed quickly with the t = 0 spectrum showing peaks corresponding to the [[M_{30}]-(3,4-lut)+2(MeCN)]$^{2+}$ and [[M_{30}]-2(lut)+2(MeCN)]$^{2+}$ fragments. The cluster continues to be present throughout the reaction time with measurements at t = 2 hours and t = 4 hours also showing these peaks (Figure S4). Mass spectrometry of crystalline **1** redissolved in a 20/80 mix of lut/MeCN shows the [Fe_{30}] cage is present with one, two and three ligands removed, with measurements repeated over a period of 24 hours showing that the molecule is present in solution for at least 1 day (Figures S5-7).

Magnetic measurements of **1** reveal relatively strong antiferromagnetic interactions between the Fe centres. The experimental dc susceptibility data (T = 2-400 K, B = 0.1 T) for **1** is plotted in Figure 3 as the χT product versus T, where χ is the molar magnetic susceptibility, T is the temperature, and B the applied magnetic field. The value of χT at T = 300 K is ~45 cm^3 K mol^{-1}, significantly lower than that expected for the sum of the Curie constants for thirty Fe^{III} (S = 5/2) ions with g_{Fe} = 2.00 (131.25 cm^3 K mol^{-1}). As the temperature decreases, the magnitude of χT decreases rapidly, reaching a value of ~3.5 cm^3 K mol^{-1} at T = 2 K, suggestive of a small/diamagnetic spin ground state. At T > 300 K, the χT value increases slowly, with no sign of an inflection or jump in value. Magnetisation data (T = 2-7 K, B = 0.5 – 7 T) appear somewhat S-shaped, with the low field data appearing to saturate at ~2 T before increasing rapidly up to ~5T, and then increasing more gradually up to 7 T. This is indicative of the presence of multiple low lying spin states, stabilised through increasing field strength.

It is computationally impossible to quantitatively analyse the magnetic data of a molecule containing 30 x S = 5/2 spins *via* conventional matrix diagonalisation techniques. Even the finite-temperature Lanczos method[18] which can approximately solve problems in Hilbert spaces with dimensions up to 10^{11} cannot be applied here. We thus resort to a classical spin model and classical Monte Carlo (CMC).[19] This allows approximations of the magnetisation and the magnitude of the exchange interactions to be obtained. Note however that classical spin models constitute a high-temperature approximation and thus can be inaccurate at (low) temperatures smaller than the typical interaction strength. Although there are nine different exchange interactions present in **1**, DFT calculations (*vide infra*) suggest they can be grouped into two categories: strongly antiferromagnetic and weakly ferro- or antiferromagnetic based on the larger Fe(tet)-O-Fe(tet/oct) angles and the smaller Fe(oct)-O-Fe(oct) angles, respectively. We therefore simplified the numerical simulations by employing a model with just two different J values representing these two different Fe-O-Fe exchange pathways. Simulations with one strong AF coupling of $-20.85 \leq J_s \leq -27.80$ cm^{-1} and one weak AF coupling of $-6.95 \leq J_w \leq -11.82$ cm^{-1} ($\hat{H} = -\sum_{i<j} J_{ij}\, \hat{\vec{s}}_i \cdot \hat{\vec{s}}_j$) come closest to replicating the magnetic observables (Figure 3), being superior to a model containing just one exchange interaction, $J = -6.95$ cm^{-1}.

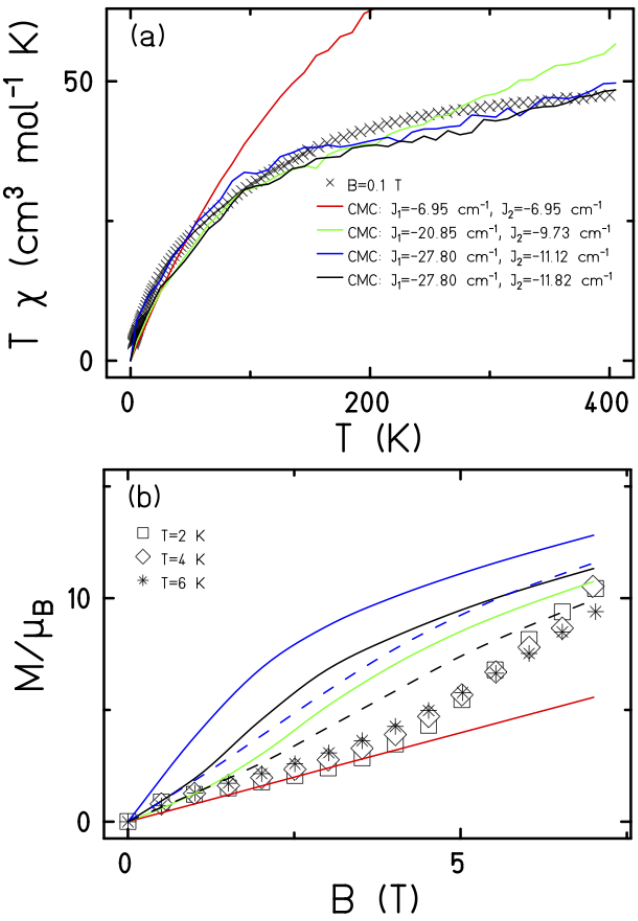

Fig. 3. (a) Plot of the χT product versus T in the 400-2 K temperature range in an applied field, B = 0.1 T. (b) Plot of M versus B in the 2-6 K range for $0.5 \leq B \leq 7$T. In the latter the solid curves are for T = 2 K, dashed curves for T = 6 K.

To further support the relative sign and magnitude of the coupling constants obtained above, we have performed DFT calculations (see the SI for the computational details) on model complexes derived from complex **1** (Figure S9). These suggest that the nine independent exchange interactions (Scheme S1; Figures S10-18 show the spin density plots) are in the range $|J| \approx$ 6-71 cm^{-1} (Table S2). All the computed exchange interactions are antiferromagnetic, with the exception of J_3' where a weak ferromagnetic exchange of +14.3 cm^{-1} has been estimated. The large antiferromagnetic interactions originate from multiple strong overlap integrals between the SOMOs of Fe^{III} centres bridged by μ_3/μ_4-O^{2-} ions (Tables S3-S11). The overlap integral is much smaller for the J_3' exchange pathway where only one dominant $d_z^2|p_z|d_z^2$ overlap integral is found (Table S7). This results in a very small contribution to the antiferromagnetic part of the interaction (J_{AF}, where $J = J_{AF} + J_F$) resulting in a small ferromagnetic interaction overall (Table S2). The results are in agreement with previous magneto-structural developed for oxo-bridged Fe^{III} complexes in which the magnitude of J is dictated by the Fe-O-Fe angle and Fe-O/Fe distances, and with the results observed for [Fe_{17}] and [Fe_{34}] in which J(tet-oct) >> J(oct-oct).[14,15]

Conclusions

The simplicity of the experimental procedure and the structural similarity of [Fe_{30}] to previously published molecules such as [Fe_{13},], [Fe_{17},] and [Fe_{34}], and to bulk oxides such as ferrihydrite, which all possess structures composed of alternating layers of tetrahedral and octahedral Fe^{III} ions, suggests

that many more molecular iron oxides must exist. The self-assembly process also suggests that multi-functional 'core-shell' species in which the Fe-oxo core is encapsulated within another (stabilising) material, *e.g*. a polyoxometalate, will be attractive targets for a diverse array of applications.

Acknowledgements

EKB thanks EPSRC for funding grants EP/P025986/1 and EP/N01331X/1. EKB/LC thank U21/EPSRC for studentships (EL, DJC).

References

1. J. Cho, S. Jeon, S. A. Wilson, L. V. Liu, E. A. Kang, J. J. Braymer, M. H. Lim, B. Hedman, K. O. Hodgson, J. S. Valentine, E. I. Solomon and W. Nam, *Nature*, 2011, **478**, 502-505.

2. J. H. Docherty, J. Peng, A. P. Dominey and S. P. Thomas, *Nature Chem*., 2017, **9**, 595–600.

3. Z. Chen, P. Li, R. Anderson, X. Wang, X. Zhang, L. Robison, L. R. Redfern, S. Moribe, T. Islamoglu, D. A. Gómez-Gualdrón, T. Yildirim, J. F. Stoddart and O.K. Farha, *Science*, 2020, **368**, 297–303.

4. R. A. Revia and M. Zhang, *Mater. Today*, 2016, **19**, 157–168.

5. C. Xie, Y. Duan, W. Xu, H. Zhang and X. Li, *Angew. Chem. Int. Ed*., 2017, **56**, 14953 –14957.

6. S. Zhu, L. Kong, L. Cao, H. Chen, M. Papaj, S. Du, Y. Xing, W. Liu, D. I. Wang, C. Shen, F. Yang, J. Schneeloch, R. Zhong, G. Gu, L. Fu, Y.-Y. Zhang, H. Ding and H.-J. Gao, *Science,* 2020, **367**, 189-192.

7. A. Sakai, S. Minami, T. Koretsune, T. Chen, T. Higo, Y. Wang, T. Nomoto, M. Hirayama, S. Miwa, D. Nishio-Hamane, F. Ishii, R. Arita and S. Nakatsuji, *Nature*, 2020, **581**, 53–57.

8. R. Lebrun, A. Ross, S. A. Bender, A. Qaiumzadeh, L. Baldrati, J. Cramer, A. Brataas, R. A. Duine and M. Kläui, *Nature*, 2018, **561**, 222–225.

9. S. Loth, S. Baumann, C. P. Lutz, D. M. Eigler and A. J. Heinrich, *Science*, 2012, **335**, 196-199.

10. L. Ye, M. Kang, J. Liu, F. von Cube, C. R. Wicker, T. Suzuki, C. Jozwiak, A. Bostwick, E. Rotenberg, D. C. Bell, L. Fu, R. Comin and J. G. Checkelsky, *Nature*, 2018, **555**, 638–642.

11. S. Ohkoshi, K. Imoto, Y. Tsunobuchi, S. Takano and H. Tokoro, *Nature Chem*., 2011, **3**, 564–569.

12. a) G. Serrano, L. Poggini, M. Briganti, A. L. Sorrentino, G. Cucinotta, L. Malavolti, B. Cortigiani, E. Otero, P. Sainctavit, S. Loth, F. Parenti, A.-L. Barra, A. Vindigni, A. Cornia, F. Totti, M. Mannini and R. Sessoli, *Nature Mater*., 2020, **19**, 546–551; b) S. L. Heath and A. K. Powell, *Angew. Chem. Int. Ed. Engl*., 1992, **31**, 191-192.

13. a) O. Sadeghi, L. N. Zakharov and M. Nyman, *Science*, 2015, **347**, 1359-1362; b) O. Sadeghi, C. Falaise, P. I. Molina, R. Hufschmid, C. F. Campana, B. C. Noll, N. D. Browning and M. Nyman, *Inorg. Chem*., 2016, **55**, 11078−11088; c) N. A. G. Bandeira, O. Sadeghi, T. J. Woods, Y.-Z. Zhang, J. Schnack, K. R. Dunbar, M. Nyman and C. Bo, *J. Phys. Chem*. *A*, 2017, **121** 1310-1318.

14. a) A. Bino, M. Ardon, D. Lee, B. Spingler and S. J. Lippard, *J. Am. Chem. Soc*., 2002, **124**, 4578−4579; b) J. van Slageren, P. Rosa, A. Caneschi, R. Sessoli, H. Casellas, Y. V. Rakitin, L. Cianchi, F. Del Giallo, G. Spina, A. Bino, A.-L. Barra, T. Guidi, S. Carretta and R. Caciuffo, *Phys. Rev. B*, 2006, **73**, 014422.

15. a) G. W. Powell, H. N. Lancashire, E. K. Brechin, D. Collison, S. L. Heath, T. Mallah and W. Wernsdorfer, *Angew. Chem. Int. Ed*., 2004, **43**, 5772−5775; b) C. Vecchini, D. H. Ryan, L. M. D. Cranswick, M. Evangelisti, W. Kockelmann, P. G. Radaelli, A. Candini, M. Affronte, I. A. Gass, E. K.

Brechin and O. Moze, *Phys. Rev. B*, 2008, **77**, 224403; c) M. Evangelisti, A. Candini, A. Ghirri, M. Affronte, G. W. Powell, I. A. Gass, P. A. Wood, S. Parsons, E. K. Brechin, D. Collison and S. L. Heath, *Phys. Rev. Lett*., 2006, **97**, 167202; d) I. A. Gass, C. J. Milios, M. Evangelisti, S. L. Heath, D. Collison, S. Parsons and E. K. Brechin, *Polyhedron*, 2007, **26**, 1835–1837; e) I. A. Gass, E. K. Brechin and M. Evangelisti, *Polyhedron*, 2013, **52**, 1177-1180.

16. A. E. Dearle, D. J. Cutler, H. W. L. Fraser, S. Sanz, E. Lee, S. Dey, I. F. Diaz-Ortega, G. S. Nichol, H. Nojiri, M. Evangelisti, G. Rajaraman, J. Schnack, L. Cronin and E. K. Brechin, *Angew. Chem. Int. Ed*., 2019, **58**, 16903-16906.

17. F. M. Michel, L. Ehm, S. M. Antao, P. L. Lee, P. J. Chupas, G. Liu, D.R. Strongin, M. A. A. Schoonen, B. L. Phillips and J. B. Parise, *Science*, 2007, **316**, 1726-1729.

18. a) J. Jaklič and P. Prelovšek, *Phys. Rev. B*, 1994, **49**, 5065-5068; b) J. Schnack and O. Wendland, *Eur. Phys. J. B*, 2010, **78**, 535-541; c) J. Schnack, J. Richter and R. Steinigeweg, *Phys. Rev. Research*, 2020, **2**, 013186.

19. C. Schröder, H. Nojiri, J. Schnack, P. Hage, M. Luban and P. Kögerler, *Phys. Rev. Lett*., 2005, 94, 017205.

Supporting Information

Synthesis

(lutH)[$Fe^{III}_{30}(\mu_4\text{-}O)_6(\mu_3\text{-}O)_{26}(\mu\text{-}OH)_{15}Br_9(lut)_{15}]Br_3$ (1)

$FeBr_3$ (0.591 g, 2 mmol) was dissolved with hexamethylenetetramine (0.476 g, 3.4 mmol) MeCN (25 ml) and 3,4-lutdine (0.35 ml, 3.1 mmol) was added. The reaction was stirred for four hours and then filtered and allowed to stand undisturbed overnight. Diffusion of iPrOH into this solution afforded dark brown plate-shaped crystals suitable for X-ray diffraction after 3 weeks. Elemental analysis (% C H N) calculated (found) for $Br_{12}C_{112}Fe_{30}H_{159}N_{16}O_{47}$: C 26.30 (25.81), N 4.38 (3.62) H 3.13 (2.84).

(Et-PyH)[$Fe^{III}_{30}(\mu_4\text{-}O)_6(\mu_3\text{-}O)_{26}(\mu\text{-}OH)_{15}Br_9(Et\text{-}py)_{15}]Br_3$·Et-py (1a)

Synthesis as for compound **1**, replacing 3,4-lutidine (0.35 ml) with 4-ethylpyridine (1 ml, 8.8 mmol) and iPrOH with diethylether. Elemental analysis (% C H N) calculated (found) for $Br_{12}C_{119}Fe_{30}H_{169}N_{17}O_{47}$: C 27.36 (26.72), N 4.56 (4.03) H 3.26 (2.95).

Single crystal X-ray crystallography

1. Single brown plate crystals of **1** were recrystallised from a mixture of acetonitrile and isopropanol by vapour diffusion. A suitable crystal with dimensions 0.15 × 0.12 × 0.04 mm^3 was selected and mounted on a MITIGEN holder in Paratone oil on a Diamond Light Source I-19 EH1 diffractometer. The crystal was kept at a steady T = 100.0 K during data collection. The structure was solved with the Superflip solution program using iterative methods and by using Olex2 as the graphical interface. The model was refined with ShelXL 2018/3 using full matrix least squares minimisation on F^2.[1,2]

1a. Single dark brown block-shaped crystals of **1a** were recrystallised from a mixture of diethyl ether and acetonitrile by vapour diffusion. A suitable crystal 0.17 × 0.09 × 0.06 mm^3 was selected and mounted on a MITIGEN holder in Paratone oil on an Rigaku Oxford Diffraction SuperNova diffractometer. The crystal was kept at a steady T = 120.0 K during data collection. The structure was solved with the ShelXT structure solution program using the Intrinsic Phasing solution method and by using Olex2 as the graphical interface. The model was refined with version 2018/3 of ShelXL using Least Squares minimisation.[1,2]

Table S1. Crystallographic information for **1** and **1a**.

Compound	**1**	**1a**
Formula	$Br_{12}C_{112}Fe_{30}H_{159}N_{16}O_{47}$	$C_{119}H_{169}Br_{12}Fe_{30}N_{17}O_{47}$
$D_{calc.}$/ g cm^{-3}	1.575	1.643
μ/mm^{-1}	3.885	19.117
Formula Weight	5115.96	5224.12
Colour	brown	dark brown
Shape	plate	block
Size/mm^3	0.15×0.12×0.04	0.17×0.09×0.06
T/K	100.0	120.0
Crystal System	monoclinic	triclinic
Space Group	*Pn*	*P*-1
Flack Parameter	0.159(10)	-
Hooft parameter	0.192(4)	-
a/Å	30.929(3)	20.7362(5)
b/Å	21.777(2)	22.7181(4)
c/Å	32.273(4)	25.0130(4)
α/°	90	95.425(2)
β/°	96.882(2)	97.928(2)
γ/°	90	113.427(2)
V/Å^3	21580(4)	10563.0(4)
Z	4	2
Z'	2	1
Wavelength/Å	0.6889	1.54178
Radiation type	Synchrotron	CuK_α
Θ_{min}/°	0.835	3.617
Θ_{max}/°	20.136	76.143
Measured Refl.	168652	174652
Independent Refl.	44728	43629
Reflections with I > 2(I)	32432	29952
R_{int}	0.0752	0.0982
Parameters	3442	2012
Restraints	9631	950
Largest Peak	0.614	1.506
Deepest Hole	-0.468	-1.245
GooF	1.038	0.984
wR_2 (all data)	0.1530	0.1791
wR_2	0.1405	0.1618
R_1 (all data)	0.0794	0.0890
R_1	0.0549	0.0633
CCDC	2105690	2105691

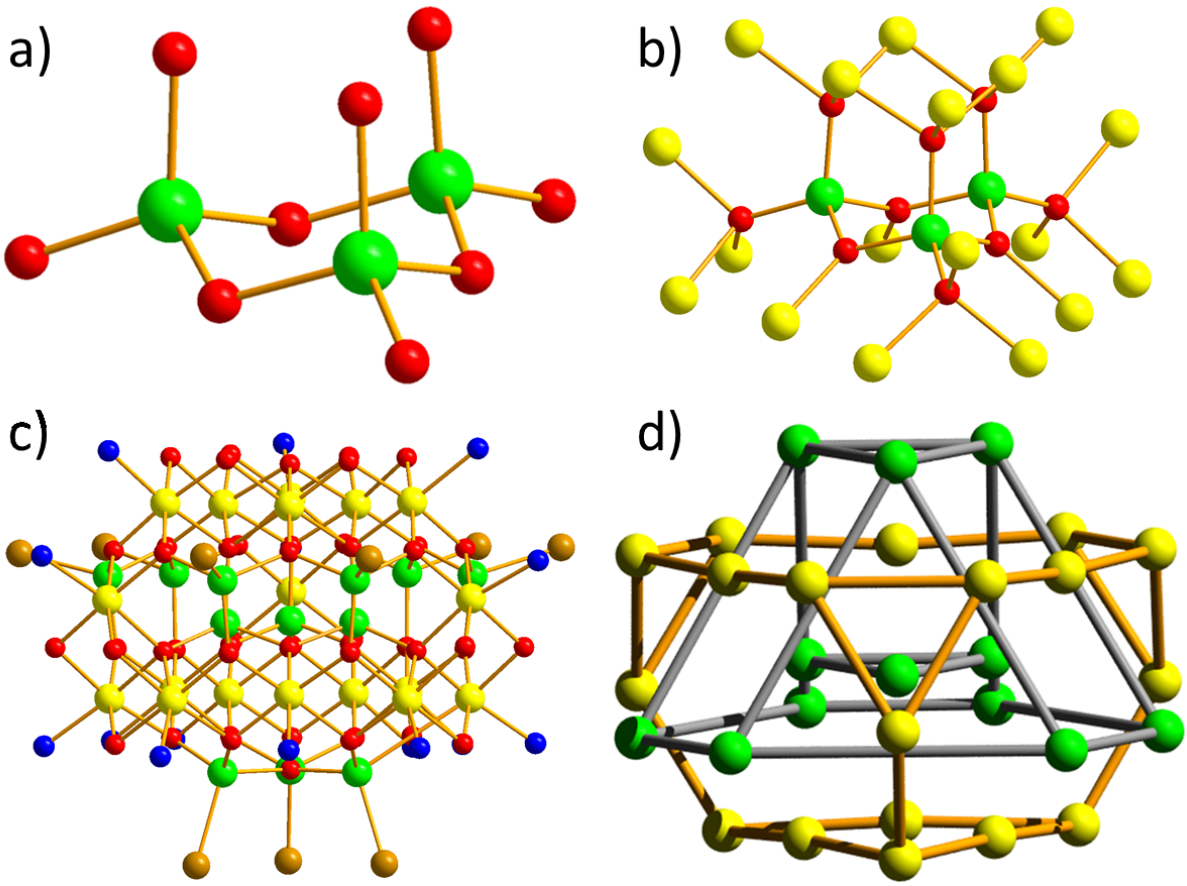

Figure S1. The metal-oxygen core in **1**, highlighting the inner $[Fe^{III}_3O_9]^{18-}$ triangle of tetrahedral Fe ions (a) linked to the $[Fe^{III}_{18}O_{22}]^{12+}$ unit of octahedral Fe ions (b), surrounded by the $[Fe^{III}_9]$ partial cuboctahedron of tetraherdal Fe ions (c). (d) Metallic skeleton. Colour code: tetrahedral Fe = green, octahedral Fe = yellow, O = red, N = blue, C = black, Br = brown. H atoms and anions omitted for clarity.

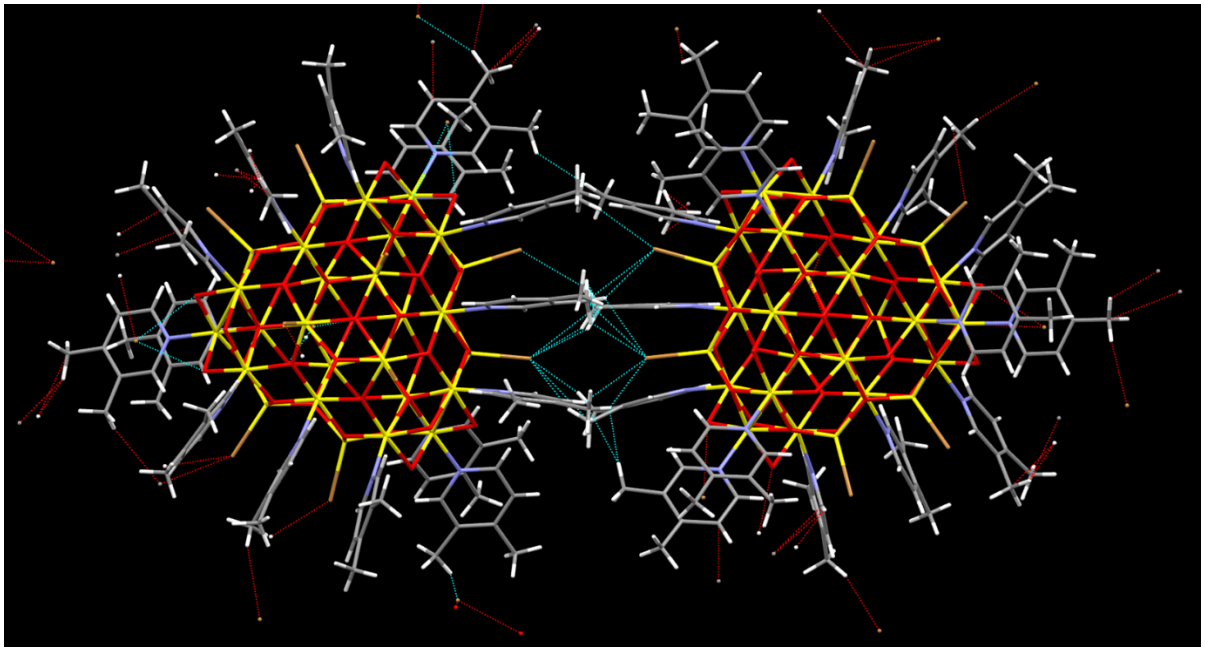

Figure S2. Closest intermolecular interactions in **1** between the lut molecules and Br ions, highlighted by the dashed blue lines at C···C/Br distances of ≥ 3.2 Å.

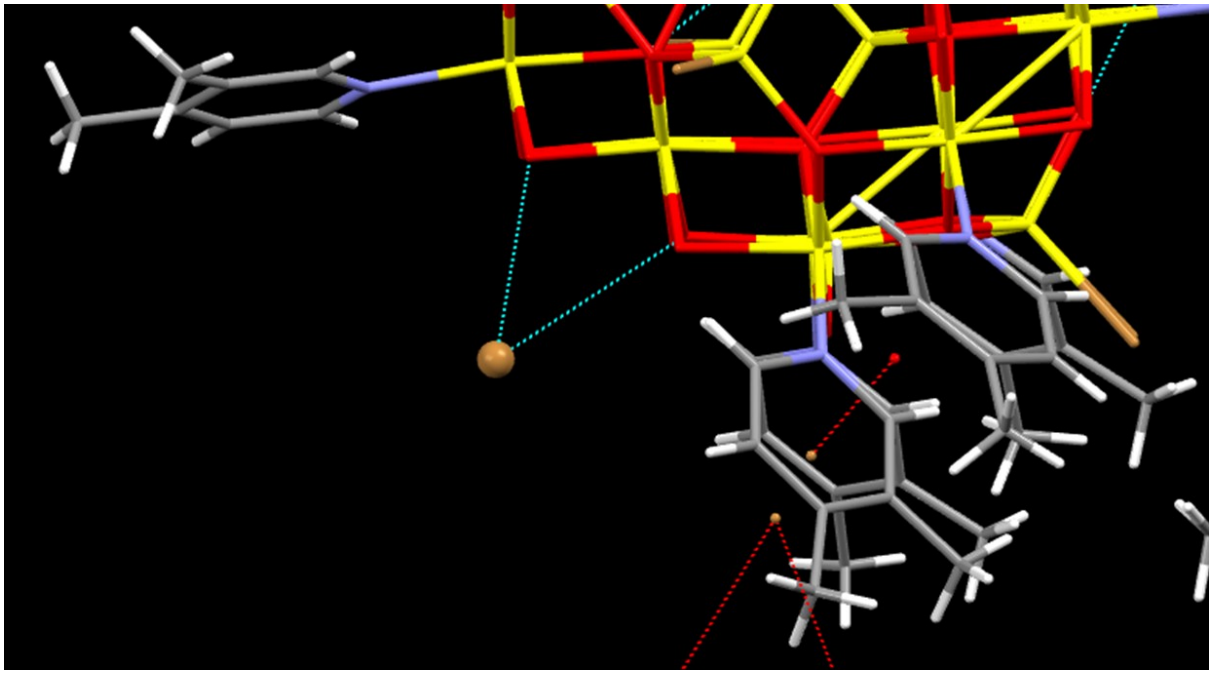

Figure S3. Close-up of the H-bond between a Br counter anion and the μ-OH ions the cluster.

Mass Spectrometry

Mass spectrometry was performed on a 7 T SolariXr FT-ICR MS (Bruker Daltonics, Bremen, Germany) with an ESI source. The spectrum was acquired in positive ion mode (ESI+). The broadband spectrum was acquired with 16 summed scans between 101 - 6000 *m*/*z*. Samples were solubilized in a 20/80 3,4-lutidine/acetonitrile mix at 230 µM and sprayed by direct infusion into the ESI source. Data were analysed using Bruker Compass DataAnalysis software. Time resolved mass spectrometry was performed on the preparatory mixture used to make **1**, under the same conditions as the re-dissolved crystalline sample. Aliquots of the reaction were taken at *t* = 0, *t* = 2 hours and *t* = 4 hours. The latter spectrum was measured after filtering the solution to remove some precipitated material. Aliquots were diluted to 230 µM (*wrt* $FeBr_3$) with a 20/80 mix of 3,4-lutidine and acetonitrile.

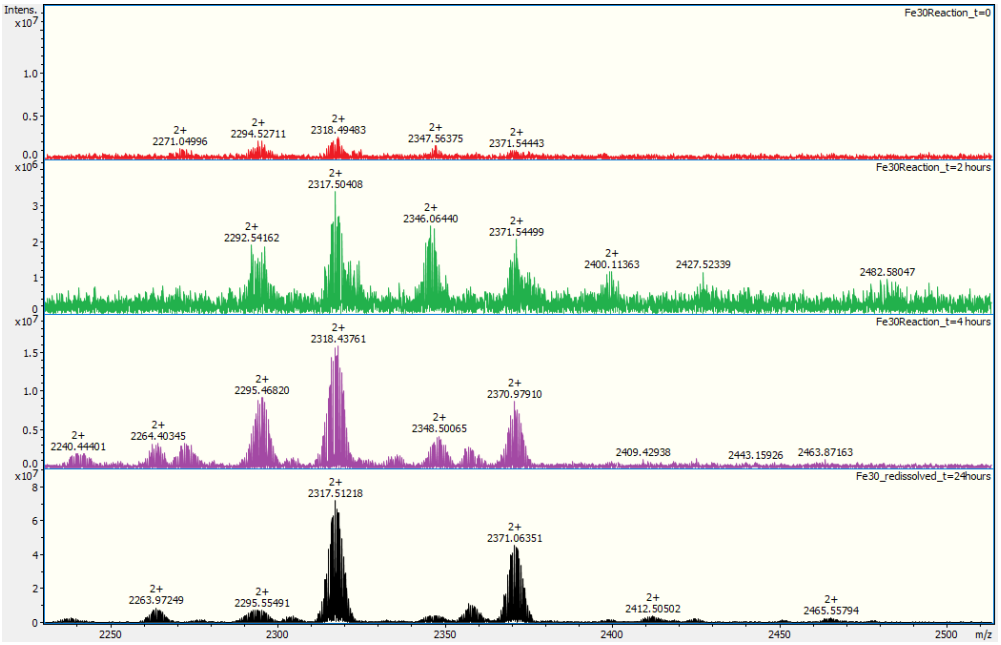

Figure S4. Time resolved mass spectra of the initial reaction mixture used to make compound **1** showing the characteristic peaks for [Fe_{30}] at 2317 and 2371 *m*/*z* at *t* = 0 (red); *t* = 2 hours (green); *t* = 4 hours (purple). The mass spectrum of crystalline **1** re-dissolved in a 20/80 mix of lut/MeCN (black) is shown for comparison.

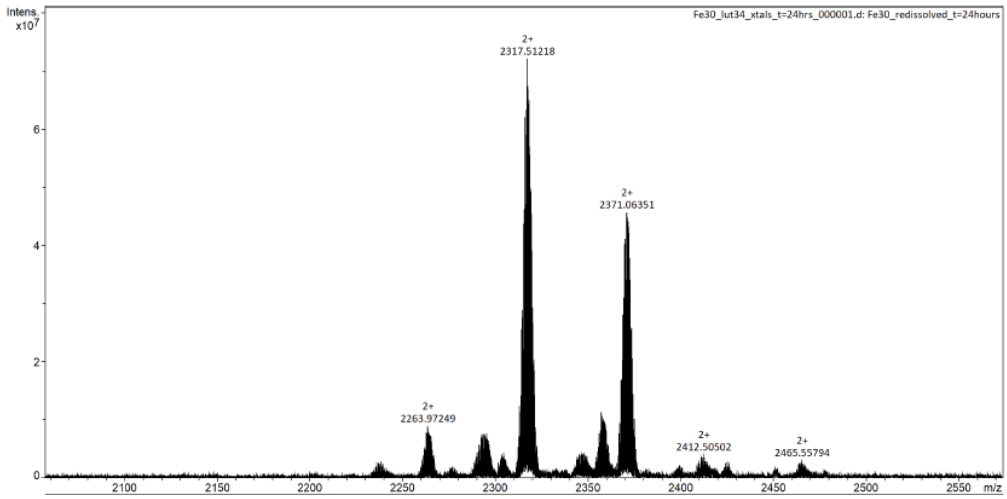

Figure S5. Mass spectrum of crystals of compound **1** re-dissolved in a 20/80 mix of lut/MeCN. The most intense peaks correspond to $[[Fe_{30}]\text{-(lut)+2(MeCN)}]^{2+}$ and $[[Fe_{30}]\text{-2(lut)+2(MeCN)}]^{2+}$ (2317 and 2371 *m*/*z* respectively). Less intense peaks correspond to fragments and adducts of [Fe30] and common MS impurities, including $[[Fe_{30}]\text{-3(lut)+2(MeCN)}]^{2+}$ (*m*/*z* = 2263), $[[Fe_{30}]\text{-2(lut)+2}(H_2O)]^{2+}$ (*m*/*z* = 2295) and $[[Fe_{30}]+(CH_3COCH_3)]^{2+}$ (*m*/*z* = 2412).

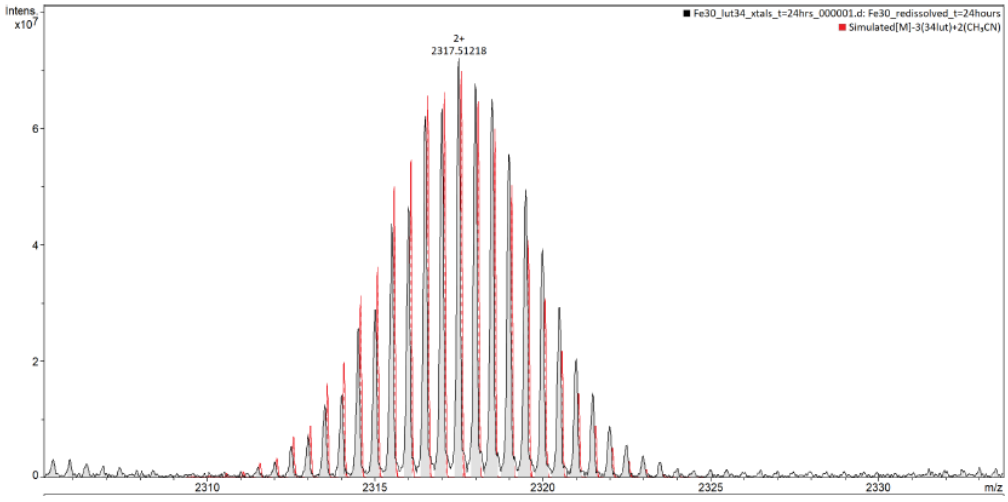

Figure S6. Mass spectrum highlighting the $[[Fe_{30}]\text{-(lut)+2(MeCN)}]^{2+}$ ion at *m*/*z* = 2317. The experimental data is in grey and the simulation in red.

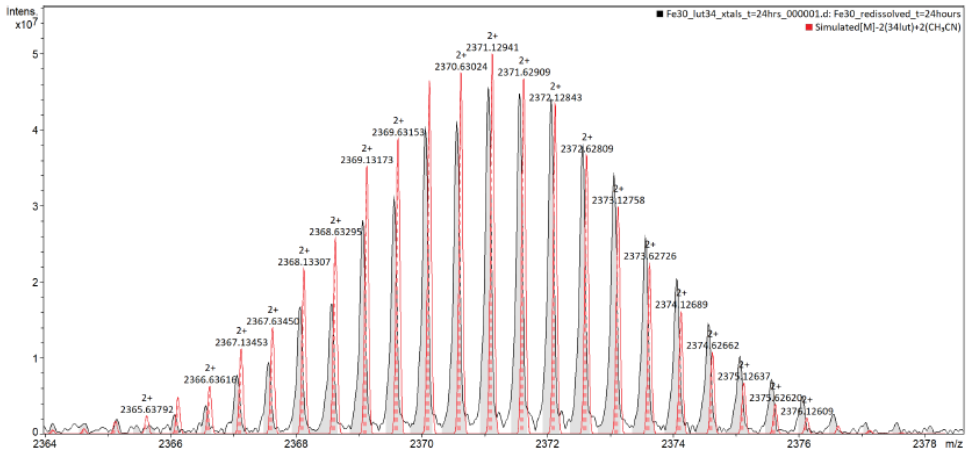

Figure S7. Mass spectrum highlighting the $[[Fe_{30}]\text{-}2(lut)+2(MeCN)]^{2+}$ ion at *m/z* = 2371. The experimental data is in grey and the simulation in red.

Computational Details

DFT calculations have been performed with the B3LYP functional using the Gaussian09 suite of programs.[3-6] The B3LYP functional is well known to provide excellent numerical accuracy in the estimation of magnetic exchange interaction values.[7,8] Here, we have estimated the pairwise exchange interactions using nine truncated models (Figure S9) as the DFT calculation is computationally expensive with complete structure of **1**. These models were constructed without altering the first coordination sphere of each pair of Fe^{III} centres, substituting neighbouring Fe^{III} sites with diamagnetic Ga^{III} ions. OH/H_2O moieties were employed for the truncated O atoms. Ahlrichs' triple-ξ plus polarisation basis set (TZVP) was used for the Fe, O, N, Br atoms and the split valence plus polarisation (SVP) basis set was used for the Ga, C and H atoms.[8] One high spin (HS, the electrons in the two Fe^{III} centres are "spin up") and one broken symmetry (BS, the electrons in one Fe(III) centre are "spin up", while those in the other are "spin down") configuration were considered for the exchange interaction, estimated using Noodleman's approach (spin-Hamiltonian (1) and (2)).[9,10] We have used the formula $J = \frac{E_{BS}-E_{HS}}{2S_1S_2+S_2}$ for the estimation of nine pairwise exchange interactions $J_1, J_2, J_2^{'}, J_3, J_3^{'}, J_3^{''}, J_4, J_5$ and $J_5^{'}$.

The following spin-Hamiltonian has been employed for the estimation of exchange coupling constant in **1**.

$$\hat{H} = -J_1\left[\hat{S}_1\hat{S}_2 + \hat{S}_1\hat{S}_3 + \hat{S}_2\hat{S}_3\right] - J_2\left[\hat{S}_1\hat{S}_4 + \hat{S}_1\hat{S}_{18} + \hat{S}_1\hat{S}_{17} + \hat{S}_1\hat{S}_{23} + \hat{S}_1\hat{S}_{25} + \hat{S}_1\hat{S}_{26} + \hat{S}_2\hat{S}_5 + \hat{S}_2\hat{S}_7 + \hat{S}_2\hat{S}_{22} + \hat{S}_2\hat{S}_{21} + \hat{S}_2\hat{S}_8 + \hat{S}_2\hat{S}_4 + \hat{S}_3\hat{S}_9 + \hat{S}_3\hat{S}_{14} + \hat{S}_3\hat{S}_{10} + \hat{S}_3\hat{S}_{29} + \hat{S}_3\hat{S}_8 + \hat{S}_3\hat{S}_{26}\right] - J_3\left[\hat{S}_{29}\hat{S}_{26} + \hat{S}_{26}\hat{S}_{25} + \hat{S}_{25}\hat{S}_{23} + \hat{S}_{25}\hat{S}_{18} + \hat{S}_{18}\hat{S}_{23} + \hat{S}_{23}\hat{S}_4 + \hat{S}_4\hat{S}_5 + \hat{S}_5\hat{S}_7 + \hat{S}_5\hat{S}_{22} + \hat{S}_7\hat{S}_{22} + \hat{S}_{22}\hat{S}_{21} + \hat{S}_7\hat{S}_8 + \hat{S}_8\hat{S}_9 + \hat{S}_9\hat{S}_{29} + \hat{S}_9\hat{S}_{10} + \hat{S}_{18}\hat{S}_{17} + \hat{S}_{29}\hat{S}_{10} + \hat{S}_{10}\hat{S}_{14}\right] - J_4\left[\hat{S}_{19}\hat{S}_{20} + \hat{S}_6\hat{S}_{24} + \hat{S}_6\hat{S}_{30} + \hat{S}_{24}\hat{S}_{30} + \hat{S}_{27}\hat{S}_{28} + \hat{S}_{11}\hat{S}_{12}\right] - J_5\left[\hat{S}_{12}\hat{S}_{21} + \hat{S}_{12}\hat{S}_{22} + \hat{S}_{12}\hat{S}_7 + \hat{S}_{12}\hat{S}_8 + \hat{S}_{11}\hat{S}_8 + \hat{S}_{11}\hat{S}_9 + \hat{S}_{11}\hat{S}_{10} + \hat{S}_{11}\hat{S}_{14} + \hat{S}_{19}\hat{S}_4 + \hat{S}_{19}\hat{S}_{23} + \hat{S}_{19}\hat{S}_{17} + \hat{S}_{19}\hat{S}_{18} + \hat{S}_{20}\hat{S}_{21} + \hat{S}_{20}\hat{S}_{22} + \hat{S}_{20}\hat{S}_4 + \hat{S}_{20}\hat{S}_5 + \hat{S}_{27}\hat{S}_{10} + \hat{S}_{27}\hat{S}_{14} + \hat{S}_{27}\hat{S}_{29} + \hat{S}_{27}\hat{S}_{26} + \hat{S}_{28}\hat{S}_{25} + \hat{S}_{28}\hat{S}_{26} + \hat{S}_{28}\hat{S}_{17} + \hat{S}_{28}\hat{S}_{18} + \hat{S}_{24}\hat{S}_4 + \hat{S}_{24}\hat{S}_{23} + \hat{S}_{24}\hat{S}_{25} + \hat{S}_{24}\hat{S}_{26} + \hat{S}_{30}\hat{S}_{26} + \hat{S}_{30}\hat{S}_{29} + \hat{S}_{30}\hat{S}_{29} + \hat{S}_{30}\hat{S}_8 + \hat{S}_{30}\hat{S}_9 + \hat{S}_6\hat{S}_4 + \hat{S}_6\hat{S}_5 + \hat{S}_6\hat{S}_7 + \hat{S}_6\hat{S}_8\right] - J_2'\left[\hat{S}_1\hat{S}_{15} + \hat{S}_1\hat{S}_{16} + \hat{S}_2\hat{S}_{13} + \hat{S}_2\hat{S}_{16} + \hat{S}_3\hat{S}_{13} + \hat{S}_3\hat{S}_{15}\right] - J_3'\left[\hat{S}_{13}\hat{S}_{16} + \hat{S}_{13}\hat{S}_{15} + \hat{S}_{15}\hat{S}_{16} + \hat{S}_{13}\hat{S}_{14} + \hat{S}_{13}\hat{S}_{21} + \hat{S}_{16}\hat{S}_{21} + \hat{S}_{16}\hat{S}_{17} + \hat{S}_{15}\hat{S}_{17} + \hat{S}_{15}\hat{S}_{14}\right] - J_3^{''}\left[\hat{S}_{27}\hat{S}_{15} + \hat{S}_{27}\hat{S}_2 + \hat{S}_{26}\hat{S}_{10} + \hat{S}_{26}\hat{S}_8 + \hat{S}_{30}\hat{S}_{10} + \hat{S}_{30}\hat{S}_{15}+\right]J_5'\left[\hat{S}_{12}\hat{S}_{13} + \hat{S}_{11}\hat{S}_{13} + \hat{S}_{15}\hat{S}_{27} + \hat{S}_{15}\hat{S}_{28} + \hat{S}_{16}\hat{S}_{19} + \hat{S}_{16}\hat{S}_{20}\right] \ldots\ldots\ldots\ldots\ldots\ldots(1)$$

The above Hamiltonian can be simplified as

$$\hat{H} = -3J_1\left[\hat{S}_{ITd}\hat{S}_{ITd}\right] - 18J_2\left[\hat{S}_{ITd}\hat{S}_{oct}\right] - 6J_2^{'}\left[\hat{S}_{ITd}\hat{S}_{oct}\right] - 18J_3\left[\hat{S}_{oct}\hat{S}_{oct}\right] - 9J_3^{'}\left[\hat{S}_{oct}\hat{S}_{oct}\right] - 6J_3^{''}\left[\hat{S}_{oct}\hat{S}_{oct}\right] - 6J_4\left[\hat{S}_{OTd}\hat{S}_{OTd}\right] - 37J_5\left[\hat{S}_{OTd}\hat{S}_{oct}\right] - 6J_5^{'}\left[\hat{S}_{OTd}\hat{S}_{oct}\right] \ldots\ldots\ldots\ldots(2)$$

Where ITd, OTd and oct denote the inner tetrahedral, outer tetrahedral and octahedral Fe^{III} centres, respectively.

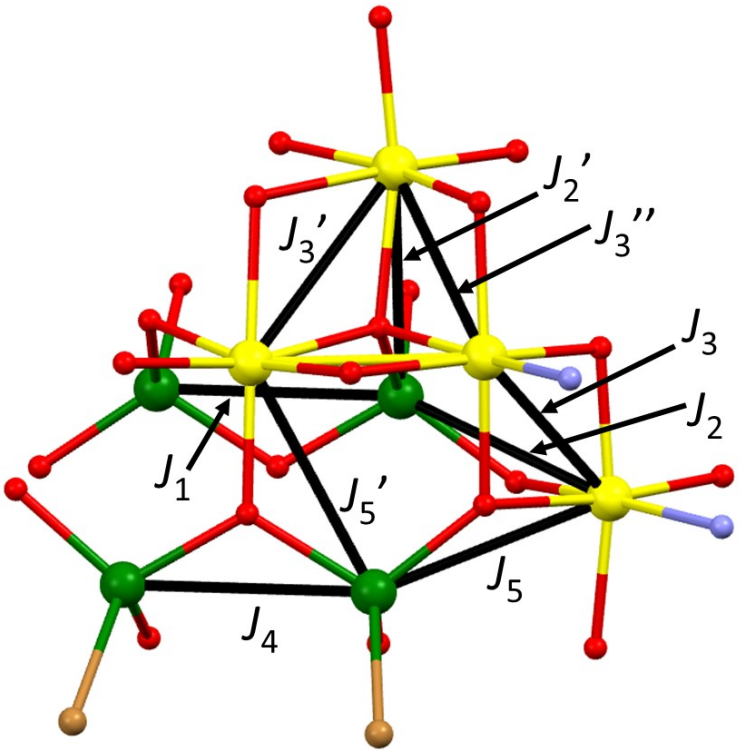

Scheme S1. Pictorial representation of the nine different magnetic exchange interactions in **1**.

	Fe-O-Fe (°)	Fe-O (Å)	Fe···Fe (Å)	J_{DFT}/ cm^{-1}
J_1	117.5	1.88	3.17	-30.6
J_2	121.2	1.93	3.36	-6.3
$J_2^{'}$	122.7	1.96	3.45	-19.2
J_3	94.9	1.97	2.92	-7.3
$J_3^{'}$	98.9	2.12	3.29	+14.3
$J_3^{''}$	99.6	2.00	3.05	-14.0
J_4	118.8	1.91	3.28	-60.0
J_5	130.3	1.89	3.44	-70.9
$J_5^{'}$	119.1	1.97	3.40	-24.9

Table S2. The nine DFT computed magnetic exchange interactions alongside the average Fe-O-Fe angles and average Fe-O and Fe···Fe distances for each interaction.

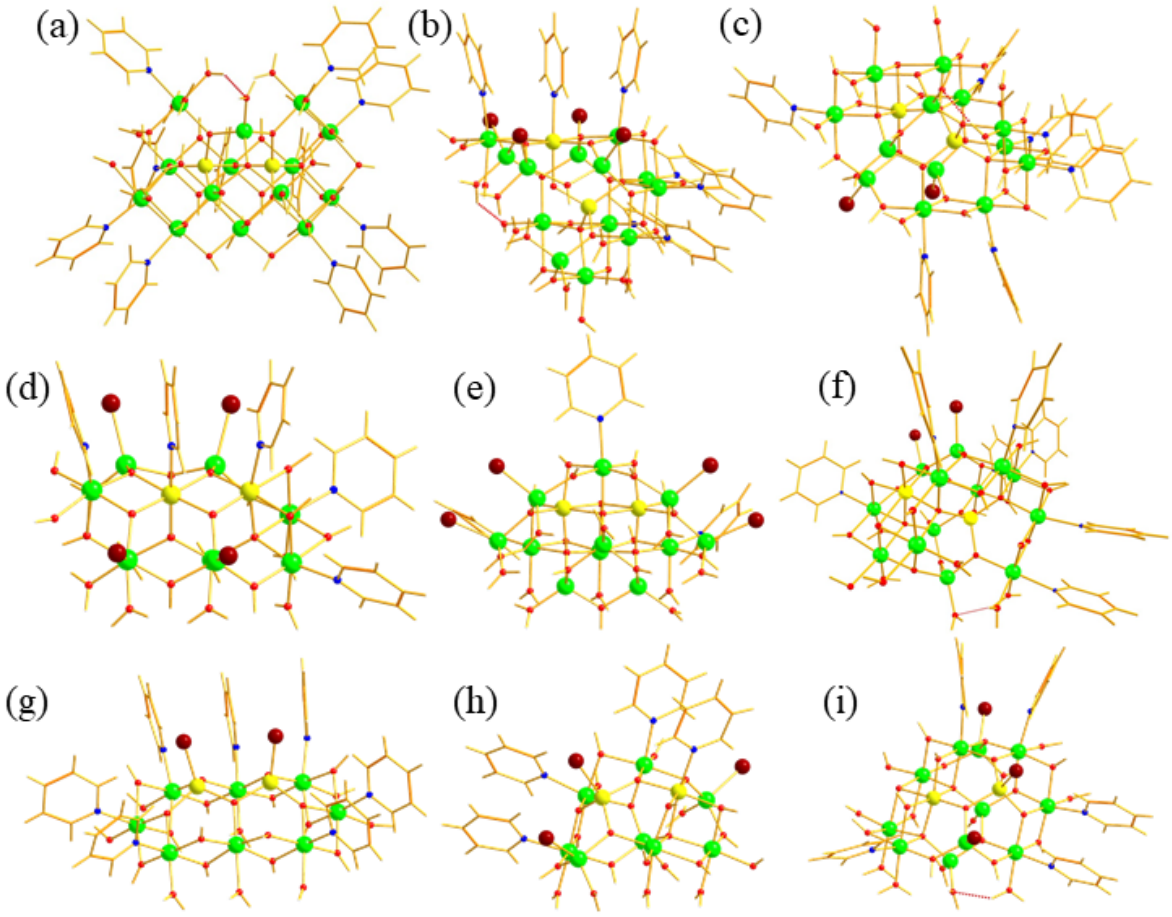

Figure S9. The nine models employed to estimate the magnetic exchange interactions in (a) J_1 (b) J_2 (c) $J_2^{'}$ (d) J_3 (e) $J_3^{'}$ (f) $J_3^{''}$ (g) J_4 (h) J_5 (i) $J_5^{'}$ exchange pathway. Colour Code: Fe – Yellow; Ga – Green; Br - Brown; O – Red; N – Blue; C – Black, H – white.

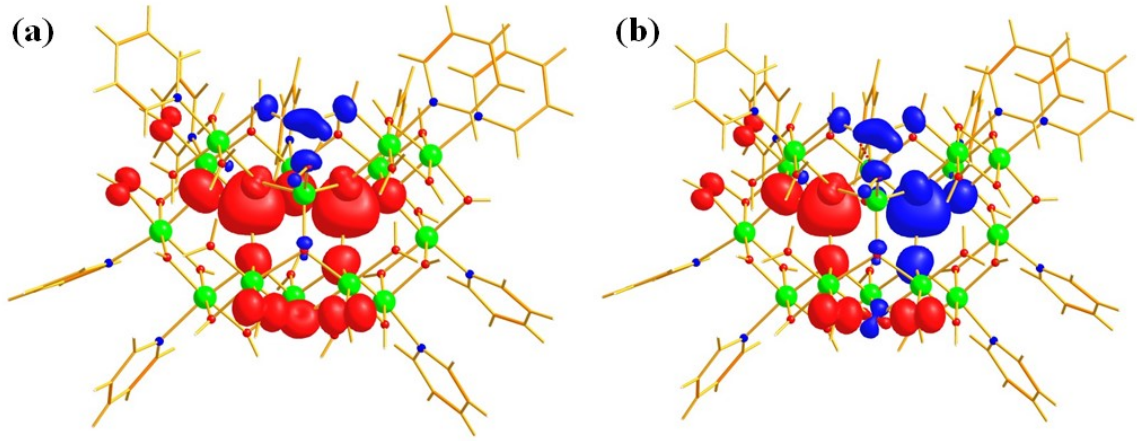

Figure S10. Spin density of the (a) HS (b) BS configurations of the model complex in the J_1 exchange pathway. The isodensity surface shown corresponds to a value of 0.006 $e^-/bohr^3$. The red and blue surfaces represent positive and negative spin density, respectively. Colour Code: Fe – Yellow; Ga – Green; Br - Brown; O – Red; N – Blue; C – Black, H – white.

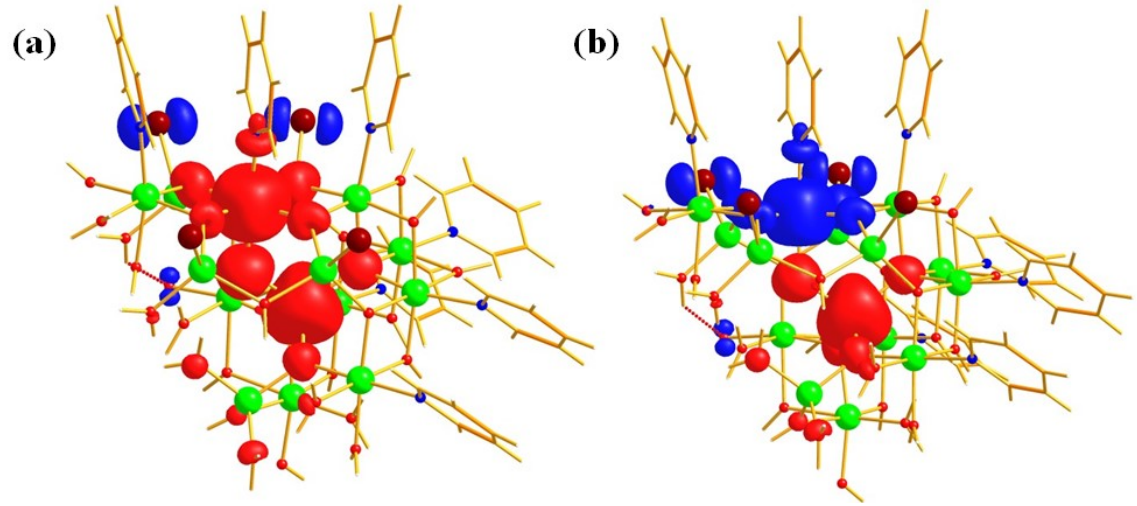

Figure S11. Spin density of the (a) HS (b) BS configurations of the model complex in the J_2 exchange pathway. The isodensity surface shown corresponds to a value of 0.006 $e^-/bohr^3$. The red and blue surfaces represent positive and negative spin density, respectively. Colour Code: Fe – Yellow; Ga – Green; Br - Brown; O – Red; N – Blue; C – Black, H – white.

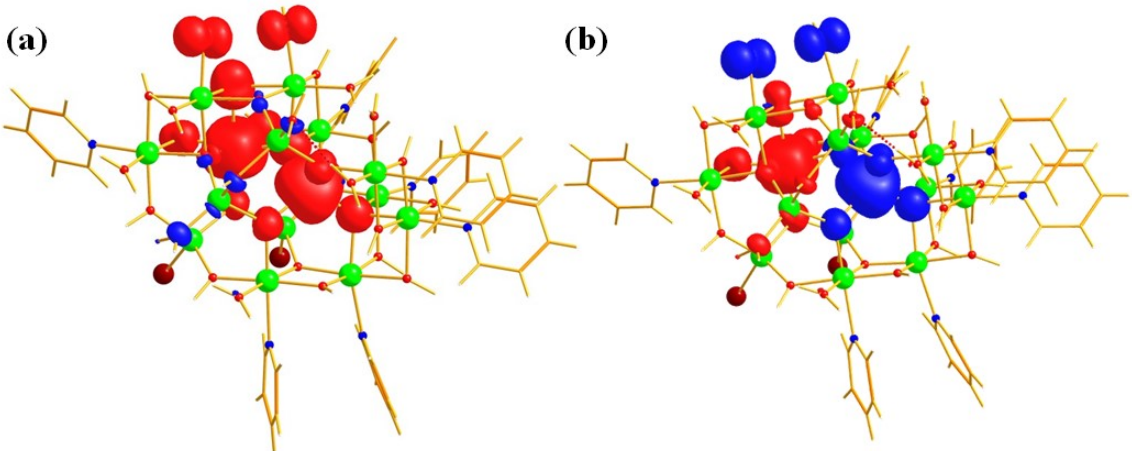

Figure S12. Spin density of the (a) HS (b) BS configurations of the model complex in the $J_2^{'}$ exchange pathway. The isodensity surface shown corresponds to a value of 0.006 e^-/bohr^3. The red and blue surfaces represent positive and negative spin density, respectively. Colour Code: Fe – Yellow; Ga – Green; Br - Brown; O – Red; N – Blue; C – Black, H – white.

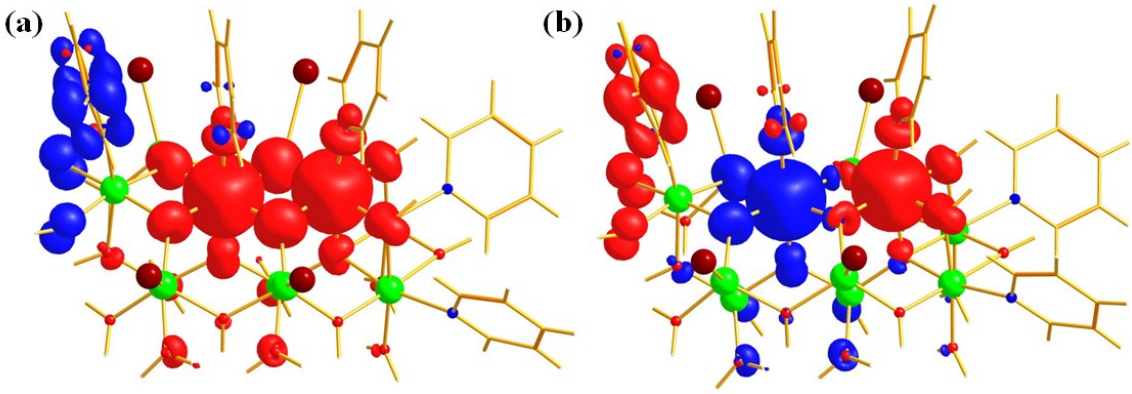

Figure S13. Spin density of the (a) HS (b) BS configurations of the model complex in the J_3 exchange pathway. The isodensity surface shown corresponds to a value of 0.006 e^-/bohr^3. The red and blue surfaces represent positive and negative spin density, respectively. Colour Code: Fe – Yellow; Ga – Green; Br - Brown; O – Red; N – Blue; C – Black, H – white.

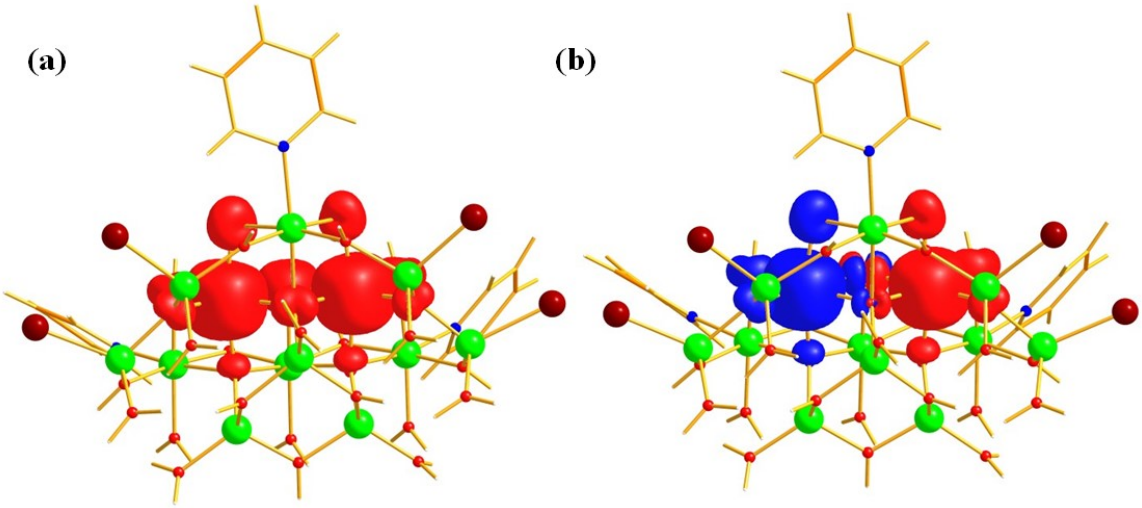

Figure S14. Spin density of the (a) HS (b) BS configurations of the model complex in the $J_3^{'}$ exchange pathway. The isodensity surface shown corresponds to a value of 0.006 e^-/bohr^3. The red and blue surfaces represent positive and negative spin density, respectively. Colour Code: Fe – Yellow; Ga – Green; Br - Brown; O – Red; N – Blue; C – Black, H – white.

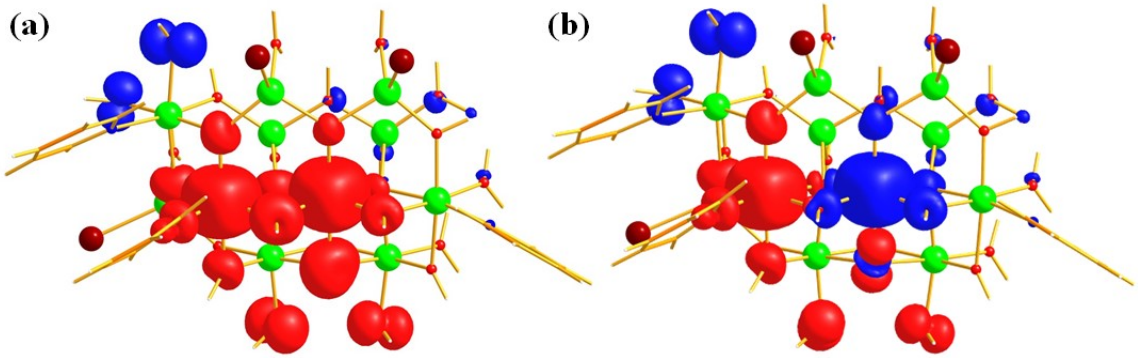

Figure S15. Spin density of the (a) HS (b) BS configurations of the model complex in the $J_3^{''}$ exchange pathway. The isodensity surface shown corresponds to a value of 0.006 e^-/bohr^3. The red and blue surfaces represent positive and negative spin density, respectively. Colour Code: Fe – Yellow; Ga – Green; Br - Brown; O – Red; N – Blue; C – Black, H – white.

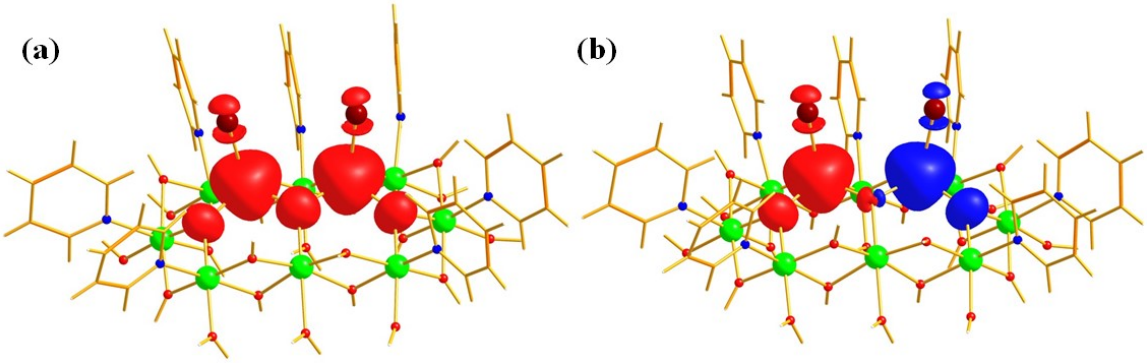

Figure S16. Spin density of the (a) HS (b) BS configurations of the model complex in the J_4 exchange pathway. The isodensity surface shown corresponds to a value of 0.006 e^-/bohr^3. The red and blue surfaces represent positive and negative spin density, respectively. Colour Code: Fe – Yellow; Ga – Green; Br - Brown; O – Red; N – Blue; C – Black, H – white.

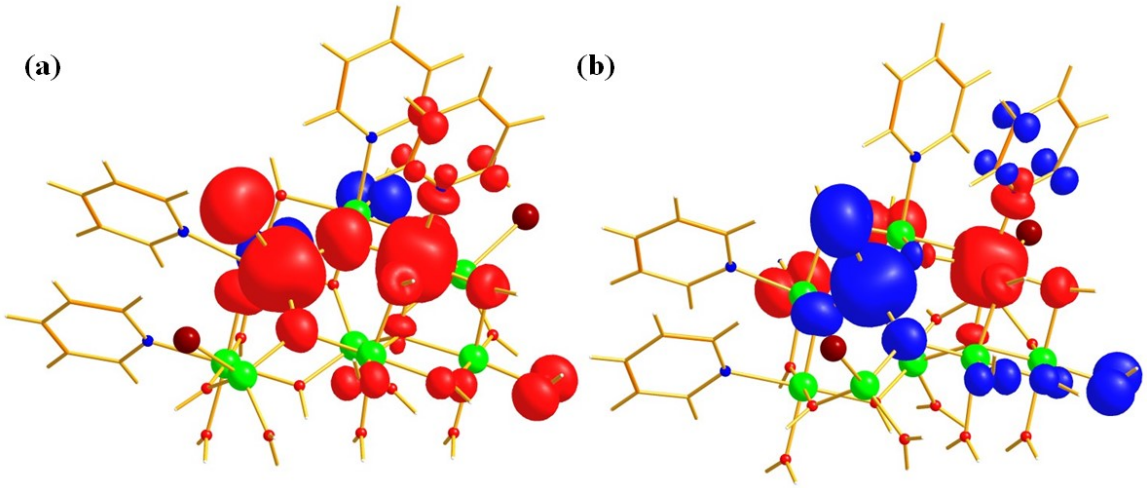

Figure S17. Spin density of the (a) HS (b) BS configurations of the model complex in the J_5 exchange pathway. The isodensity surface shown corresponds to a value of 0.006 e^-/bohr^3. The red and blue surfaces represent positive and negative spin density, respectively. Colour Code: Fe – Yellow; Ga – Green; Br - Brown; O – Red; N – Blue; C – Black, H – white.

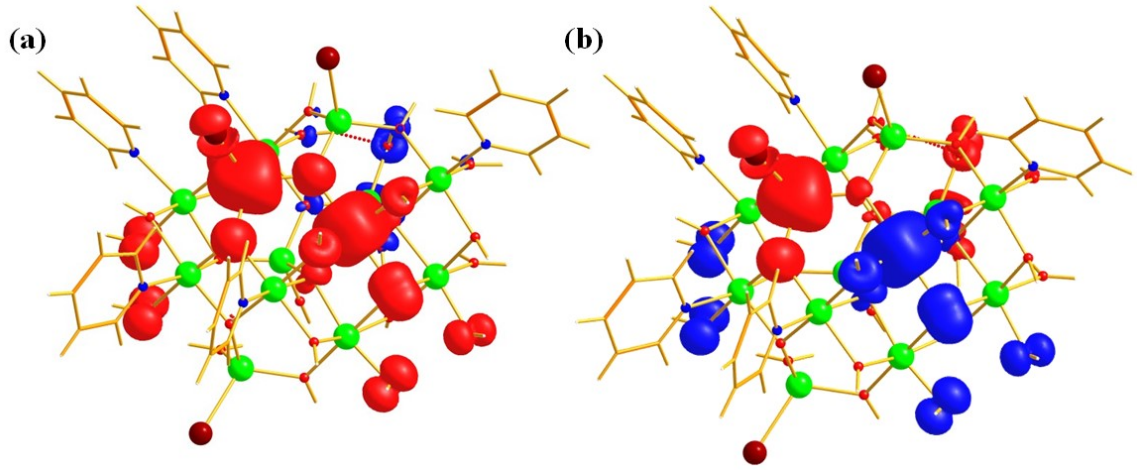

Figure S18. Spin density of the (a) HS (b) BS configurations of the model in the $J_5^{'}$ exchange pathway. The isodensity surface shown corresponds to a value of 0.006 e^-/bohr^3. The red and blue surfaces represent positive and negative spin density, respectively. Colour Code: Fe – Yellow; Ga – Green; Br - Brown; O – Red; N – Blue; C – Black, H – white.

Table S3. Overlap integrals between the SOMOs of the two Fe^{III} centres in the J_1 exchange pathway.

Beta→ Alpha↓	d_{z2}	d_{xz}	d_{yz}	d_{x2-y2}	d_{xy}
d_{xz}	-0.122	0.132	-0.216	-0.223	0.095
d_{yz}	0.030	0.057	0.040	0.108	-0.071
d_{x2-y2}	-0.048	0.013	-0.012	0.236	-0.028
d_{xy}	0.026	-0.081	0.018	0.042	-0.029
d_{z2}	-0.007	0.121	0.046	0.017	-0.038

Table S4. Overlap integrals between the SOMOs of the two Fe^{III} centres in the J_2 exchange pathway.

Beta→ Alpha↓	d_{z2}	d_{yz}	d_{xz}	d_{x2-y2}	d_{xy}
d_{z2}	-0.010	-0.179	-0.019	-0.018	-0.029
d_{yz}	-0.018	-0.069	0.114	0.176	0.080
d_{xz}	-0.001	0.058	-0.012	-0.002	-0.062
d_{x2-y2}	0.030	0.268	-0.036	0.162	-0.025
d_{xy}	0.050	-0.017	-0.051	-0.019	0.232

Table S5. Overlap integrals between the SOMOs of the two Fe^{III} centres in $J_2^{'}$ exchange pathway.

Beta→ Alpha↓	d_{z2}	d_{yz}	d_{xz}	d_{x2-y2}	d_{xy}
d_{z2}	-0.059	0.111	-0.090	0.037	-0.022
d_{yz}	-0.137	-0.091	-0.192	0.068	0.028
d_{xz}	0.120	0.044	-0.002	0.022	-0.018
d_{x2-y2}	0.098	0.062	-0.041	-0.026	-0.019
d_{xy}	-0.227	-0.168	0.002	0.130	-0.060

Table S6. Overlap integrals between the SOMOs of the two Fe^{III} centres in the J_3 exchange pathway.

Beta→ Alpha↓	d_{xy}	d_{x2-y2}	d_{xz}	d_{z2}	d_{yz}
d_{z2}	-0.138	0.259	0.144	-0.080	0.046
d_{yz}	0.104	-0.216	0.138	0.014	-0.045
d_{xz}	0.241	0.091	-0.104	0.055	0.057
d_{x2-y2}	0.198	0.187	-0.149	0.122	-0.025
d_{xy}	0.012	0.140	-0.110	-0.078	-0.081

Table S7. Overlap integrals between the SOMOs of the two Fe^{III} centres in the $J_3^{'}$ exchange pathway.

Beta→ Alpha↓	d_{yz}	d_{x2-y2}	d_{xz}	d_{xy}	d_{z2}
d_{yz}	-0.006	-0.049	0.069	-0.017	-0.065
d_{xz}	0.107	0.086	-0.056	0.028	-0.159
d_{x2-y2}	0.040	0.049	-0.101	-0.192	-0.040
d_{xy}	-0.152	-0.077	-0.113	0.185	-0.048
d_{z2}	-0.128	-0.041	-0.123	0.058	-0.261

Table S8. Overlap integrals between the SOMOs of the two Fe^{III} centres in the $J_3^{''}$ exchange pathway.

Beta→ Alpha↓	d_{z2}	d_{yz}	d_{xz}	d_{x2-y2}	d_{xy}
d_{z2}	0.326	0.013	-0.091	0.033	0.079
d_{yz}	0.211	0.001	-0.161	0.090	0.040
d_{xz}	0.074	-0.006	-0.098	-0.297	-0.003
d_{x2-y2}	-0.037	-0.071	0.139	0.057	-0.125
d_{xy}	-0.095	-0.000	-0.016	-0.140	0.009

Table S9. Overlap integrals between the SOMOs of the two Fe^{III} centres in the J_4 exchange pathway.

Beta→ Alpha↓	d_{xy}	d_{x2-y2}	d_{xz}	d_{yz}	d_{z2}
d_{xy}	0.189	0.204	-0.084	0.045	-0.053
d_{x2-y2}	-0.140	-0.050	-0.036	0.099	0.024
d_{xz}	0.365	0.038	0.022	0.068	0.081
d_{z2}	0.027	0.163	0.014	0.053	-0.075
d_{yz}	0.217	0.039	-0.236	0.003	0.099

Table S10. Overlap integrals between the SOMOs of the two Fe^{III} centres in the J_5 exchange pathway.

Beta→ Alpha↓	d_{x2-y2}	d_{xy}	d_{z2}	d_{xz}	d_{yz}
d_{xy}	-0.037	0.285	0.014	0.001	-0.066
d_{yz}	0.116	-0.043	-0.107	-0.099	-0.162
d_{x2-y2}	0.071	-0.180	0.103	-0.051	-0.102
d_{xz}	-0.221	-0.188	-0.099	-0.236	0.043
d_{z2}	0.174	0.148	0.014	-0.132	-0.126

Table S11. Overlap integrals between the SOMOs of the two Fe^{III} centres in the $J_5^{'}$ exchange pathway.

Beta→ Alpha↓	d_{z2}	d_{yz}	d_{xz}	d_{xy}	d_{x2-y2}
d_{z2}	-0.096	0.046	0.109	0.010	0.010
d_{yz}	0.070	0.044	-0.002	-0.018	0.022
d_{xz}	0.145	0.091	-0.192	0.028	0.068
d_{xy}	-0.087	-0.168	0.002	-0.060	0.130
d_{x2-y2}	0.203	0.062	-0.041	-0.019	-0.026

References

1. G. M. Sheldrick, *Acta Crystallogr. Sect. C: Cryst. Struct. Commun.,* 2015, **71**, 3-8.
2. O. V. Dolomanov, L. J. Bourhis, R. J. Gildea, J. A. K. Howard and H. Puschmann, *J. Appl. Crystallogr.* 2009, **42**, 339-341.
3. M. J. Frisch, G. W. Trucks, H. B. Schlegel, G. E. Scuseria, M. A. Robb, J. R. Cheeseman, G. Scalmani, V. Barone, G. A. Petersson, H. Nakatsuji, X. Li, M. Caricato, A. Marenich, J. Bloino, B. G. Janesko, R. Gomperts, B. Mennucci, H. P. Hratchian, J. V. Ortiz, A. F. Izmaylov, J. L. Sonnenberg, D. Williams-Young, F. Ding, F. Lipparini, F. Egidi, J. Goings, B. Peng, A. Petrone, T. Henderson, D. Ranasinghe, V. G. Zakrzewski, J. Gao, N. Rega, G. Zheng, W. Liang, M. Hada, M. Ehara, K. Toyota, R. Fukuda, J. Hasegawa, M. Ishida, T. Nakajima, Y. Honda, O. Kitao, H. Nakai, T. Vreven, K. Throssell, J. A. Montgomery Jr., J. E. Peralta, F. Ogliaro, M. Bearpark, J. J. Heyd, E. Brothers, K. N. Kudin, V. N. Staroverov, T. Keith, R. Kobayashi, J. Normand, K. Raghavachari, A. Rendell, J. C. Burant, S. S. Iyengar, J. Tomasi, M. Cossi, J. M. Millam, M. Klene, C. Adamo, R. Cammi, J. W. Ochterski, R. L. Martin, K. Morokuma, O. Farkas, J. B. Foresman, D. J. Fox, Gaussian 09, Revision A.02, Gaussian Inc., Wallingford CT, 2016.
4. D. Becke, *J. Chem. Phys*., 1993, **98**, 5648–5652.
5. A. Schäfer, H. Horn and R. Ahlrichs, *J. Chem. Phys*., 1992, **97**, 2571–2577.
6. A. Schäfer, C. Huber and R. Ahlrichs, *J. Chem. Phys*., 1994, **100**, 5829–5835.
7. H. W. L. Fraser, L. Smythe, S. Dey, G. S. Nichol, S. Piligkos, G. Rajaraman, E. K. Brechin, *Dalton Trans*., 2018 , **47**, 8100-8109.
8. M. M. Hänninen, A. J. Mota, R. Sillanpää, S. Dey, G. Velmurugan, G. Rajaraman and E. Colacio, *Inorg. Chem*., 2018, **57**, 3683–3698.
9. L. Noodleman, *J. Chem. Phys*., 1981, **74**, 5737–5743.
10. E. Ruiz, J. Cano, S. Alvarez and P. Alemany, *J. Comput. Chem*., 1999, **20**, 1391-1400.